Structural Features of *Clostridium botulinum* Neurotoxin Subtype A2 Cell Binding Domain

Kyle S. Gregory [1], Tejaswini B. Mahadeva [1], Sai Man Liu [2] and K. Ravi Acharya [1,*]

[1] Department of Biology and Biochemistry, University of Bath, Claverton Down, Bath BA2 7AY, UK; kg540@bath.ac.uk (K.S.G.); tejaswini.brahmadevarahalli.mahadeva@bath.edu (T.B.M.)

[2] Protein Sciences Department, Ipsen Bioinnovation Limited, 102 Park Drive, Milton Park, Abingdon OX14 4RY, UK; sai.man.liu@ipsen.com

[*] Correspondence: bsskra@bath.ac.uk; Tel.: +44-(0)1225-386238

Abstract: Botulinum neurotoxins (BoNT) are a group of clostridial toxins that cause the potentially fatal neuroparalytic disease botulism. Although highly toxic, BoNTs are utilized as therapeutics to treat a range of neuromuscular conditions. Several serotypes (BoNT/A-/G, /X) have been identified with vastly differing toxicological profiles. Each serotype can be further sub-categorised into subtypes due to subtle variations in their protein sequence. These minor changes have been attributed to differences in both the duration of action and potency for BoNT/A subtypes. BoNTs are composed of three domains—a cell-binding domain, a translocation domain, and a catalytic domain. In this paper, we present the crystal structures of the botulinum neurotoxin A2 cell binding domain, both alone and in complex with its receptor ganglioside GD1a at 1.63 and 2.10 Å, respectively. The analysis of these structures reveals a potential redox-dependent Lys-O-Cys bridge close to the ganglioside binding site and a hinge motion between the H_{CN} and H_{CC} subdomains. Furthermore, we make a detailed comparison with the previously reported H_C/A2:SV2C structure for a comprehensive structural analysis of H_C/A2 receptor binding.

Keywords: botulinum neurotoxin; cell-binding domain; subtype A2; crystal structure; ganglioside binding; redox switch

Key Contribution: Three-dimensional crystal structures of the cell-binding domain subtype A2 of *Clostridium botulinum* neurotoxin type A (the most common serotype used in clinical therapy) both alone and in complex with GD1a ganglioside are presented in this paper. These two molecular structures reveal important features of ganglioside recognition for this subtype.

1. Introduction

Botulinum neurotoxins (BoNTs), although highly toxic, are now routinely used as therapeutics with over 100 medicinal applications [1]. They function by cleaving soluble *N*-ethylmaleimide-sensitive factor attachment protein receptor (SNARE) proteins, halting the release of acetylcholine at the neuromuscular junction (NMJ) resulting in flaccid paralysis [2]. This makes them exceptional candidates for the treatment of a range of neuromuscular disorders, and advancements in biotechnology have resulted in the further expansion of their therapeutic potential [3,4]. Several immunologically distinct BoNT serotypes produced by *Clostridium botulinum* (BoNT/A-/G, /X) have been identified [5], with a growing number of subtypes (e.g., BoNT/A1, /A2, and /A3) that arise due to subtle variations in amino acid sequences [6]. Furthermore, BoNT-like molecules have also been identified in non-clostridial species, such as *Weissella oryzae* [7], *Enterococcus faecium* [8,9], and *Paraclostridium bifermentans* [10]. The substantial number and varying toxicological profiles of BoNT serotypes and subtypes provide opportunities of developing fine-tuned medicines for specific applications.

BoNTs are expressed as a single polypeptide chain that must be cleaved post-translationally into the active di-chain, consisting of an N-terminal Light Chain (LC) and a C-terminal Heavy Chain (HC) held together by a single disulphide bond. The LC is a Zn^{2+}-endopeptidase domain, whereas the HC comprises two domains—an N-terminal translocation domain (H_N) and a C-terminal cell binding domain (H_C) [11]. Understanding how each domain contributes to toxicity will aid in the development of BoNT molecules for medicinal applications. For BoNT/A, the H_C/A binds to both a ganglioside (e.g., GD1a) and synaptic vesicle protein 2 (SV2C) [12] at the nerve terminals of the neuromuscular junction. Upon binding, the molecule is internalized by endocytosis. Subsequently, in response to the acidic environment of the endosome, the H_N/A undergoes conformational change that results in the translocation of the LC/A across the endosomal membrane [13–16]. Once in the cytosol, LC/A is released by reduction in the disulphide bond [17] so that it may cleave its target SNARE protein, a 25 kDa Synaptosomal-Associated Protein (SNAP-25) [18].

Considering that the H_C domain has been shown to contribute to BoNT potency [19], the determination of the precise molecular interactions across the BoNT-ganglioside interface, as well as the associated conformational changes that occur upon binding, may reveal features that contribute to variation in toxicity across BoNT serotypes and subtypes [20–22]. Previous structures (PDB: 5MOYand 6ES1) of H_C/A2 in complex with its protein receptor, SV2C (H_C/A2:SV2C), revealed conformational changes mostly to SV2C itself [23,24]. In this paper, we present the crystal structures of H_C/A2 alone and also in complex with GD1a receptor oligosaccharide (H_C/A2:GD1a) and describe the key residues involved with ganglioside binding, and the conformational changes that occur. Furthermore, we observed a 'significant' hinge motion between the H_{CC} and H_{CN} subdomains when compared to reported structures H_C/A2:SV2C, and note a potential redox-dependent Lys-O-Cys bridge close to the ganglioside binding site (GBS).

2. Results and Discussion

2.1. Structure of H_C/A2

The structure of H_C/A2 was determined to a resolution of 1.63 Å (Table 1) by molecular replacement. It has an N-terminal β-jelly roll fold and a C-terminal β-trefoil (Figure 1A) that is consistent with other H_C/A subtypes [25–27]. The quality of the electron density map is good throughout except for a small loop region (Arg 1269-Phe 1277). This loop (which is conserved across all BoNT/A subtypes) precedes the ganglioside binding site (GBS) and appears to be disordered for other H_C/A subtypes [28,29]. This is likely due to the inherent flexibility of this loop so that it can accommodate ganglioside binding.

Table 1. X-ray crystallographic data collection and refinement statistics for the structures of H_C/A2 alone and in complex with GD1a. Outer shell statistics are in parenthesis.

Beamline	I04	I04
Wavelength	0.9795 Å	0.9795 Å
Protein	**H_C/A2**	**H_C/A2:GD1a**
Crystallographic statistics		
Space group	P 2_1 2_1 2_1	P 4_1
Unit cell dimensions a, b, c (Å) α, β, γ (°)	39.92, 100.79, 116.15 90, 90, 90	105.07, 105.07, 132.58 90, 90, 90
Resolution range (Å)	116.15–1.63 (1.66–1.63)	105.07–2.10 (2.14–2.10)
R_{merge}	0.159 (5.530)	0.246 (3.916)
R_{pim}	0.031 (1.087)	0.048 (0.847)
$<I/\sigma(I)>$	11.6 (0.7)	11.1 (0.9)

Table 1. *Cont.*

$CC_{1/2}$	0.999 (0.299)	0.999 (0.400)
Completeness (%)	100.00 (99.90)	100.00 (100.00)
No. observed reflections	1,563,838 (77,009)	2,288,498 (4633)
No. unique reflections	59,567 (2930)	83,782 (4633)
Multiplicity	26.3 (26.3)	27.3 (21.9)
Refinement Statistics		
R_{work}/R_{free}	0.205/0.233	0.189/0.227
RMSD bond lengths (Å)	0.011	0.010
RMSD bond angles (°)	1.53	1.61
Ramachandran plot statistics (%) Favoured Allowed Outliers	96.00 4.00 0.00	95.00 5.00 0.00
Average B-Factors (Å2) Protein atoms Solvent atoms GD1a ligand	32.80 32.52 36.94 N/A	48.6 44.98 46.24 84.2
No. Atoms Protein Solvent GD1a	3606 3372 234 N/A	7143 6733 333 77
PDB code	**7Z5T**	**7Z5S**

2.2. Structure of H_C/A2 in Complex with GD1a Receptor Ganglioside

The structure of H_C/A2:GD1a complex was solved by molecular replacement to 2.1 Å (Table 1) with two molecules (A and B) in the asymmetric unit (Figure 1B). Clear positive difference map electron density was observed at the GBS of molecule B that could be readily modelled as GD1a, whereas for molecule A, the GBS is inaccessible to GD1a due to crystal packing. Therefore, the H_C/A2:GD1a asymmetric unit contains both the GD1a-bound and unbound states of H_C/A2. A total of 5/6 monosaccharides are clearly defined by the electron density (Figure 1C). GD1a forms a total of 10 hydrogen bonding interactions to H_C/A2, two of which are water-mediated (Figure 2). This binding mode is identical to what was observed in H_C/A3, with the exception of Trp 1266, which binds Sia^6 in H_C/A2:GD1a, but is unmodelled in H_C/A3:GD1a [28].

The superimposition of molecule 'A' and 'B' (for C_α atoms) yields an RMSD of 0.47 Å, indicating that the overall structure of the molecule does not change upon binding GD1a. However, the loop spanning residues 1269–1277 appears to widen upon GD1a binding—the distance between the C_α atoms of residues 1269 and 1277 is ~4.5 Å greater in molecule B than that in molecule A (Figure 1D). This change in loop positioning is accompanied by the rotation of Phe 1278 towards the GBS, a feature that has been observed previously in the H_C/A3:GD1a, H_C/A4:GD1a, and H_C/A5:GM1b structures [26,28]. This residue, along with Phe 1117 and Phe 1252, forms a hydrophobic pocket occupied by Sia^5 (Figure 1E).
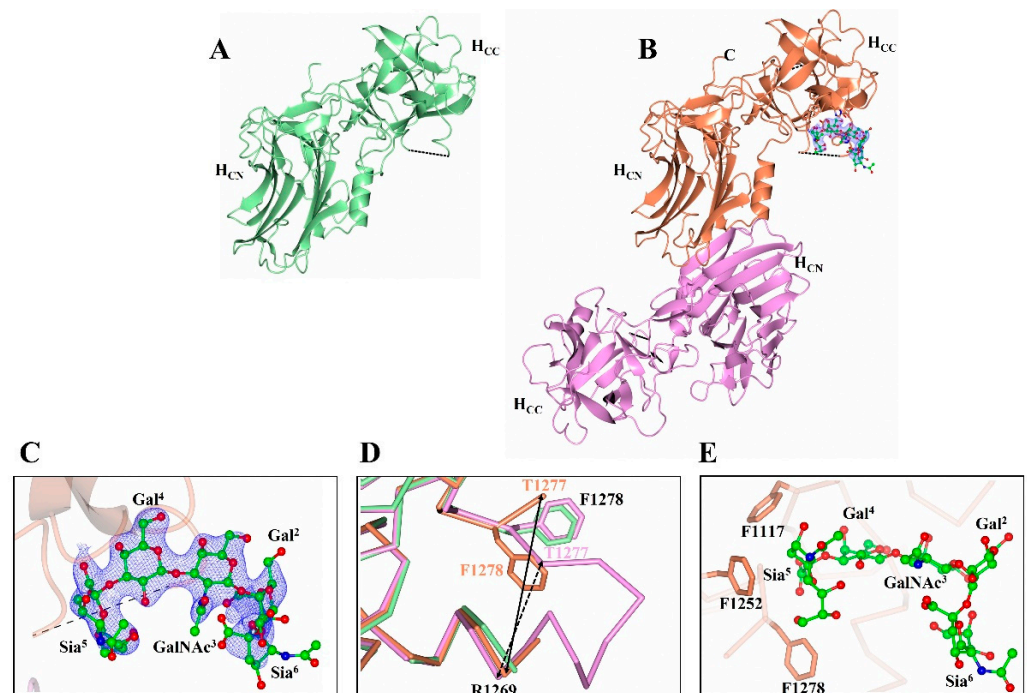
Figure 1. Structure of botulinum neurotoxin A2 cell-binding domain. (**A**) Crystal structure of H$_C$/A2 (pale green). (**B**) Crystal structure of H$_C$/A2 in complex with GD1a (H$_C$/A2:GD1a). (Molecule B is displayed in orange, and molecule A in magenta.) (**C**) Electron density map (2Fo-Fc) of GD1a contoured to 1 σ level. (**D**) Opening of the R1269-T1277 loop upon binding, and associated flip of F1278. The difference in Cα distance between R1269 and T1277 of molecule A and B is highlighted by a solid and dotted arrow, respectively. (**E**) Hydrophobic pocket formed by F1117, F1252, and F1278 that binds GD1a (ball and stick). Dashed lines indicate unmodelled regions.
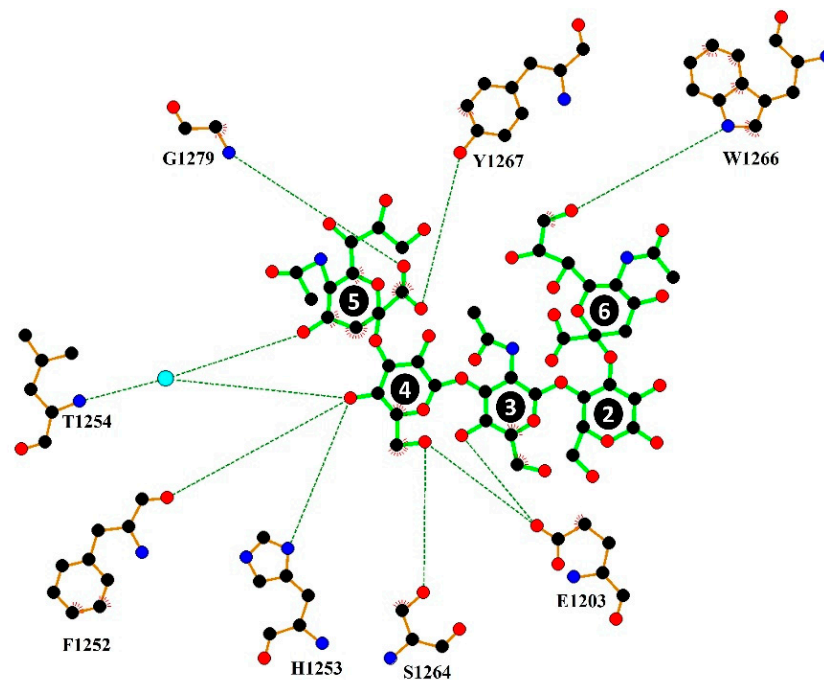
Figure 2. Ligplot+ representation of H$_C$/A2:GD1a interactions. Hydrogen bonding interactions are represented by a dotted line. The cyan sphere indicates a water-molecule-mediated interaction. The first glucose was not modelled due to weak electron density, 2 & 4 = galactose, 3 = *N*-acetylgalactosamine 5 & 6 = sialic acid.

2.3. H_C/A2 Is Primed for Receptor Binding

The conformational changes that occur with H_C/A2 upon the binding of GD1a are highlighted in Figure 3. The residues Phe 1252 and Phe 1272 moved towards the GBS and contribute to a hydrophobic patch, while the movement of His 1253 can be attributed to the formation of a hydrogen bond with Gal[4] (Figure 3B). Compared to a previous structure of H_C/A2 in complex with SV2C (PDB: 5MOY [23]), the superimposition of C_α atoms gave an RMSD of 0.96 Å, indicating that the structure does not drastically alter conformation upon SV2C binding (Figure 4A). There are few changes that occur at the residue level across the H_C/A2:SV2C interface upon binding (Figure 4B,C); however, there are noticeable differences in the conformation of two loop regions at residues 1164–1172 and 1225–1236. For the former loop, the differences are due to crystal packing, whereas for the latter loop, the variation is likely due to the inherent flexibility as residues 1228 and 1229 could not be modelled. Similar findings were also observed with another reported structure of H_C/A2:SV2C (PDB: 6ES1 [24]) (not shown). Taken together, the analysis of the ganglioside and SV2C binding sites suggest H_C/A2 is primed to bind its receptors, requiring minimal conformational change.
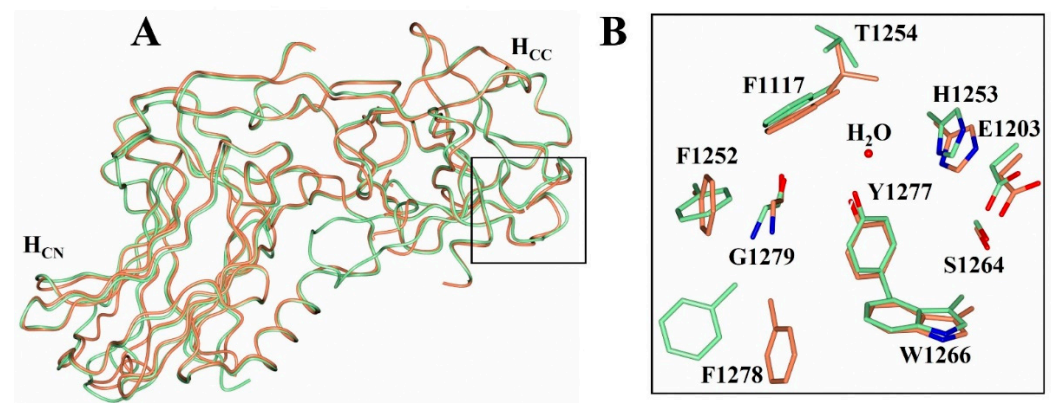
Figure 3. Structural comparison of H_C/A2 and H_C/A2:GD1a. (**A**) Superimposition of C_α atoms of H_C/A2 (pale green) and H_C/A2:GD1a (orange). The ganglioside binding site (GBS) is highlighted by the box. (**B**) Residues comprising the GBS before (pale green) and after binding to GD1a (orange).
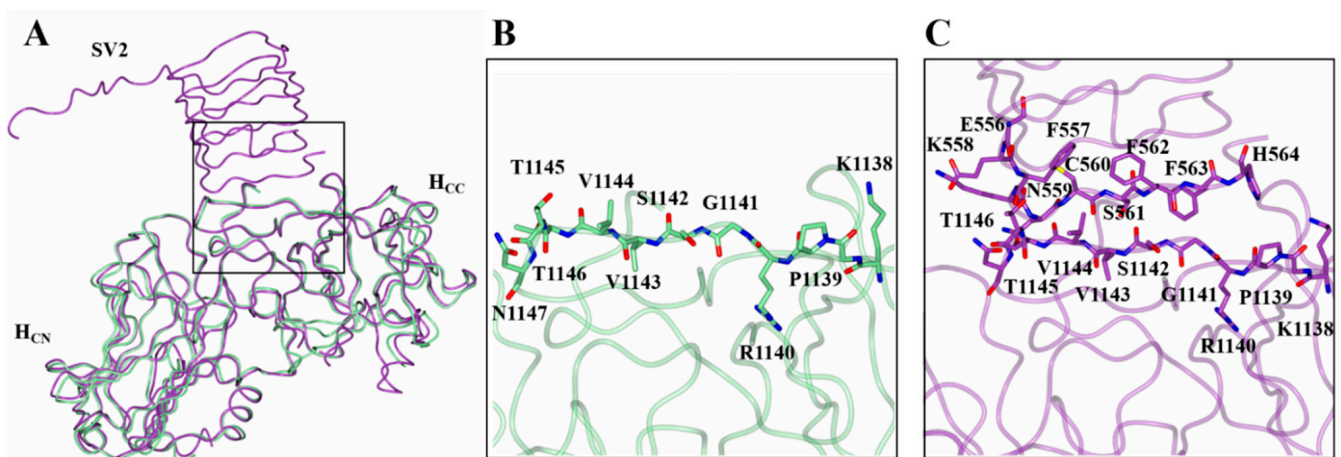
Figure 4. Structural comparison of H_C/A2 and H_C/A2:SV2C. (**A**) Global superimposition of C_α atoms of H_C/A2 (pale green) and H_C/A2:SV2C (purple; PDB: 5MOY). (**B**) Residues of the H_C/A2 SV2C binding site, indicating the position of key residues (sticks) prior to binding. (**C**) Residues of the H_C/A2 SV2C binding interface, indicating the position of key residues (sticks) after binding.

2.4. Hinge Motion between the H_{CN} and H_{CC} Subdomain

The superimposition of $H_C/A2$:GD1a and $H_C/A2$:SV2C structures with the $H_C/A2$ structure revealed a slight misalignment across the entirety of the C_α trace (RMSD values of 0.79 Å and 0.99 Å, respectively). The superimposition of just the C-terminal subdomains (H_{CC}) showed a nearly identical alignment, with the N-terminal subdomain (H_{CN}) rotated out of position relative to each other (Figure 5). Using DynDom (which estimates domain motions in proteins) [30], the $H_{CN}/A2$ subdomain appears to rotate 3.6° in one direction when bound to GD1a (Figure 5A), but 6.7° in the other direction when bound to SV2C (Figure 5B). This hinge-like motion is not believed to facilitate SV2C receptor binding because it does not alter the position of the key binding residues. However, considering that the H_{CC} subdomain is responsible for anchoring BoNT to the NMJ cell membrane, it is possible that the hinge between H_{CC} and H_{CN} may aid in the orientation of the H_N and LC towards the membrane in preparation for translocation, which is consistent with what has been proposed previously [31].
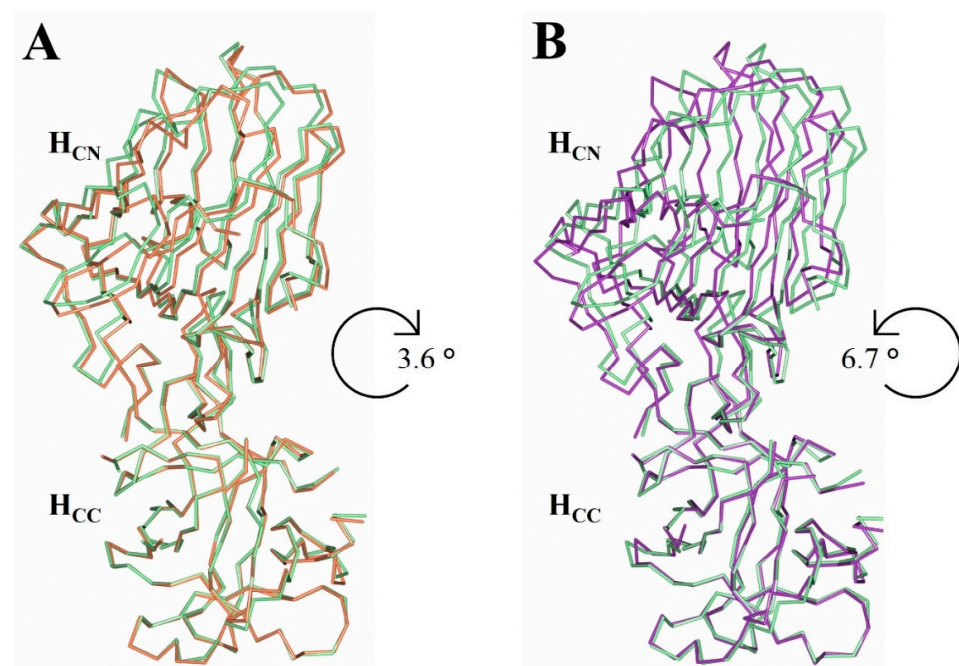
Figure 5. Hinge motion between the H_{CN} and H_{CC} subdomain. Superimposition of the H_{CC} subdomain of $H_C/A2$ alone (pale green) with $H_C/A2$ in complex with GD1a (orange) (**A**) or SV2C (purple; PDB: 5MOY) (**B**) indicates the presence of a hinge motion between the H_{CC} and H_{CN} subdomains.

2.5. Lys 1236-X-Cys 1280 Bridge near the GBS

In both the $H_C/A2$ and $H_C/A2$:GD1a structures, clear electron density was observed between Lys 1236 and Cys 1280 (Figure 6A,B) indicating the presence of an unusual covalent bridge between the two residues. A similar observation was made in the structure of $H_C/A5$ involving equivalent residues [27]. The Lys-X-Cys bridge is a recently reported interaction that may be a widespread phenomenon in many protein structures [32,33]. There are two possible bridging atoms where X is either an O or a C (as a methylene group, CH_2). The formation of an -O- bridge occurs via the spontaneous oxidation of the cystine sulfhydryl group in the absence of reducing agents, whereas the formation of a $-CH_2-$ bridge has been suggested to occur by the reaction of a Lys with CO_2 or CH_2O [32,34].

Both possibilities were modelled into the electron density of the $H_C/A2$ structure and refined (Figure 7A,B). However, it was not possible to determine the identity of the bridging atom; crystallographically, both were equally possible (Figure 7A–C). This illustrates the difficulty in determining the precise nature of the bridging atom, and there appears to be a divided debate on this topic [35].
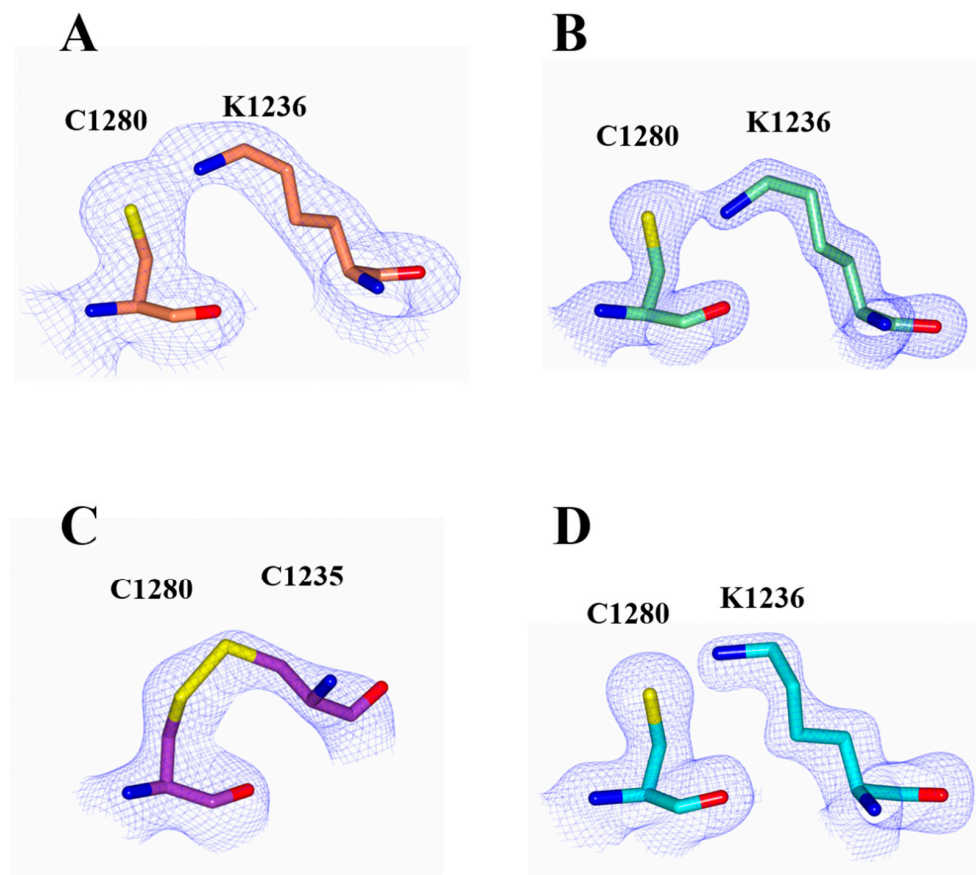
Figure 6. Lys 1236-X-Cys 1280 Bridge. (**A**) 2Fo-Fc electron density (contoured to 1 σ) was observed between C1280 and K1236 of H$_C$/A2 when bound to GD1a (H$_C$/A2:GD1a) (**A**) and alone (H$_C$/A2) (**B**), which indicated the presence of a Lys-X-Cys bridge. When bound to SV2C, however, one structure (PDB: 6ES1) showed the formation of a disulphide bond between C1280 and C1235 (**C**) and another (PDB: 5MOY) showed no electron density between these two residues (**D**).

On the other hand, the previously reported crystal structures of H$_C$/A2 bound to SV2C showed either the formation of a disulphide bond between Cys 1280 and Cys 1235 instead (Figure 6C), or no interaction between the two residues (Figure 6D). Interestingly, both of these structures (PDB: 6ES1 and 5MOY, respectively) were determined from crystals grown under reducing conditions, in contrast to the present structure of H$_C$/A2 where crystals were grown under non-reducing conditions. This indicates that the formation of the Lys-X-Cys bridge may be dependent on the redox environment. This type of redox-dependency has been observed previously in the transaldolase enzyme from the *Neisseria gonorrhoeae* bacterium, where a Lys-O-Cys bridge serves as an allosteric redox switch [36].

Further, a recent report based on a systematic study on the presence of Lys-Cys bridges in protein structures revealed that oxygen is the most likely bridging atom [33]; therefore, we modelled this atom in the final deposited coordinates.

Although the biological relevance of this Lys 1236-O-Cys 1280 bridge in the present H$_C$/A2 structure is currently unknown, it is interesting to note that both these equivalent residues are conserved in all subtypes of BoNT/A, and that they are situated in a dynamic region of the protein close to the GBS. Cys 1280 is located close to Phe 1277, whose sidechain is known to flip orientation upon ganglioside binding, and Lys 1236 is positioned within a β-hairpin (residues 1220–1240) that appears to possess a flexible loop based on the lack of electron density for residues 1224–1236 (Figure 8). Further investigation will be required to confirm the identity and biological function (if any) of this Lys-O-Cys bridge.
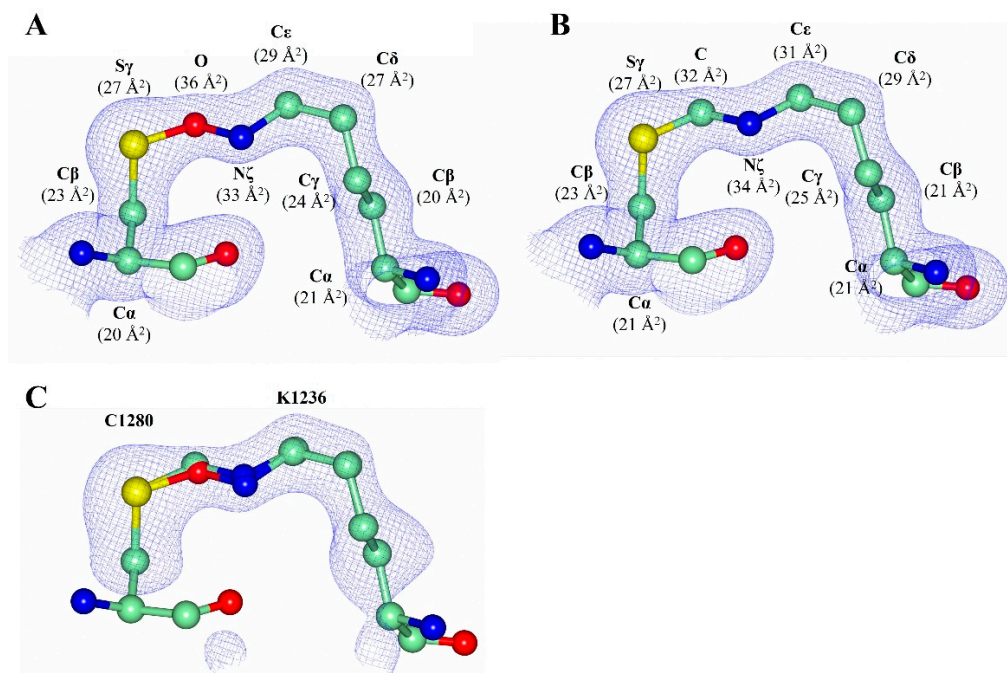
Figure 7. Analysis of the Lys 1236-X-Cys 1280 bridge in $H_C/A2$ (present structure). (**A**) The 2Fo-Fc map (contoured at 1 σ level) of Lys-X-Cys modelled as Lys-O-Cys; the B-factors for each atom across the bridge are displayed. (**B**) The 2Fo-Fc map (contoured at 1 σ level) of Lys-X-Cys modelled as Lys-CH_2-Cys; the B-factors for each across the bridge are displayed. (**C**) Omit map for Lys 1236 and Cys 1280 side chains, contoured at 3 σ level.
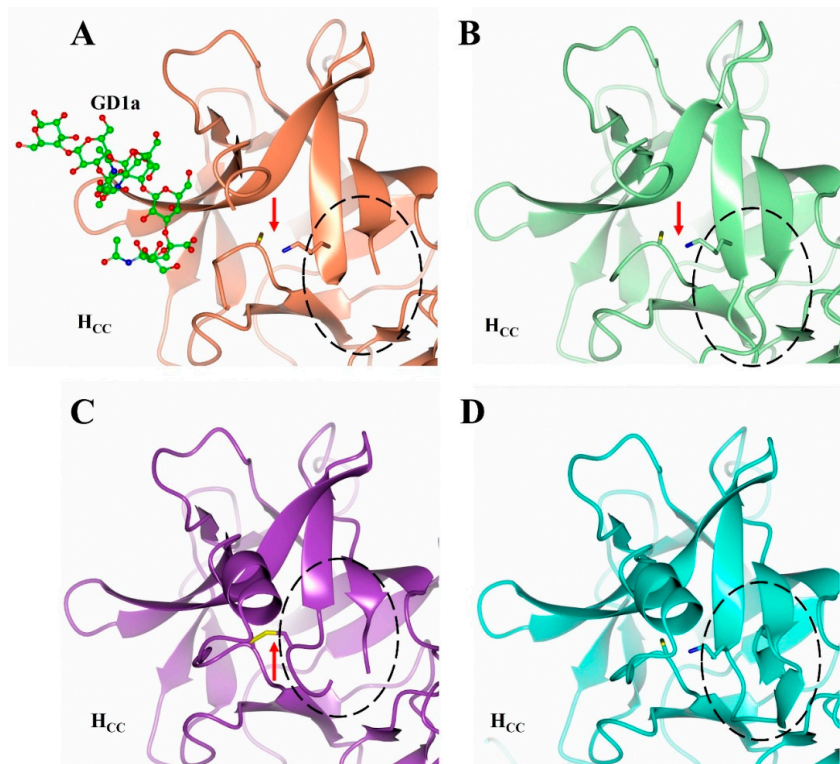
Figure 8. Conformational changes associated with the Lys-X-Cys bridge. Comparison of the structure of the 1220–1240 β-hairpin of $H_C/A2$ alone (**B**), in complex with GD1a (**A**), and bound to SV2C ((**C**), PDB: 5MOY; and (**D**), PDB: 6ES1). The 1224–1236 loop is highlighted by the dotted circle, and the red arrow indicates the location of the bridging interaction (either Lys-X-Cys or Cys-Cys).

3. Conclusions

The crystal structures of H_C/A2 alone and in complex with GD1a reveal a total of 9 residues that form 10 hydrogen bonding interactions with the sugar moiety, accompanied by a conformational change of a loop (residues 1269–1277) located near the GBS. Furthermore, structural comparison with H_C/A2 bound to its protein receptor, SV2C, revealed features not previously reported in the literature. The H_{CN} and H_{CC} subdomains appear to rotate about a common hinge position depending on which receptor molecule H_C/A2 binds—ganglioside or SV2C. This motion may be involved in orienting the translocation domain towards the cell surface following dual-receptor-initiated endocytosis. We also note the presence of a Lys 1236-O-Cys 1280 bridge in the two crystal structures of H_C/A2 presented here that is located on a loop near the GBS. The biological significance of both the hinge and Lys-O-Cys bridge is unknown and requires further investigation. This information might be valuable in the bioengineering and manufacture of BoNT/A subtypes for enhanced therapeutic applications.

4. Materials and Methods

4.1. Expression and Purification of H_C/A2

The pJ401 vector containing H_C/A2 (BoNT/A2 residues 871–1296) was transformed into One Shot BL21 (DE3) Star competent cells (Thermo Fisher Scientific, Loughborough, UK), as previously described [37]. Cultures were grown in TB at 37 °C until an OD_{600} of 0.6, and protein expression was induced with 1 mM IPTG at 16 °C for at least 16 h. Cells were lysed in 50 mM Tris pH 7.4, 20 mM imidazole, and 0.5 M NaCl. H_C/A2 was captured by Ni^{2+} affinity chromatography and eluted with 0.5 M imidazole in 50 mM Tris pH 7.4, 0.5 M NaCl via a gradient elution. H_C/A2 was further purified by gel filtration using a superdex 200 column into a final buffer of 50 mM Tris pH 7.4, and 150 mM NaCl. The purified protein was flash frozen in liquid nitrogen for storage at −20 °C until required for crystallisation.

4.2. X-ray Crystallography

Crystals of H_C/A2 and H_C/A2:GD1a were grown using the sitting drop vapour diffusion method at concentrations of 17 mg/mL and 8 mg/mL, respectively. For the latter, H_C/A2 was incubated with 5 mM GD1a for at least 1 h prior to setting up crystallisation screens. H_C/A2 crystals grew at 16 °C in 0.1 M Sodium acetate, pH 4.5, 22% *v/v* PEG smear broad (4.55% PEG 400, 4.55% PEG 500 MME, 4.55% PEG 600, 4.55% PEG 1000, 4.55% PEG 2000, 4.55% PEG 3350, 4.55% PEG 4000, 4.55% PEG 5000, 4.55% PEG 6000, 4.55% PEG 8000, and 4.55% PEG 10,000), whereas H_C/A2:GD1a crystals grew at 16 °C in 0.2 M lithium citate tribasic tetrahydrate, 20% *w/v* PEG 3350. Crystals were mounted into a cryoloop and flash frozen in liquid nitrogen. Diffraction data were collected on I04 beamline at Diamond Light Source (Oxon, UK). A total of 7200 images were collected at 0.1° oscillation with exposure times of 0.01 s, for both H_C/A2 and H_C/A2:GD1a crystals. Data processing was carried out in DIALS [38] and both structures were determined by molecular replacement using PHASER [39] as part of the CCP4 package [40]. The H_C/A2:SV2C (PDB: 5MOY) structure (excluding the coordinates for SV2C) was used as a search model for H_C/A2 [23], and the refined H_C/A2 structure was subsequently used as a search model for H_C/A2:GD1a. Both structures were refined using REFMAC [41] and Phenix [42], with modelling performed in COOT [43]. The structures were validated using Molprobity [44] and PDB validation [45]. Figures were produced using CCP4mg [46].

Author Contributions: K.S.G. performed all crystallographic analysis, wrote the manuscript, and supervised T.B.M.; T.B.M. expressed and purified H_C/A2 and performed crystallographic analysis of H_C/A2; S.M.L. analyzed the data and edited the manuscript; K.R.A. supervised the study, analyzed the data, and edited the manuscript. All authors have read and agreed to the published version of the manuscript.

References

1. Evidente, V.G.H.; Adler, C.H. An update on the neurologic applications of botulinum toxins. *Curr. Neurol. Neurosci. Rep.* **2010**, *10*, 338–344. [CrossRef] [PubMed]
2. Monteucucco, C.; Schiavo, G.; Rossetto, O. The mechanism of action of tetanus and botulinum neurotoxins. *Arch. Toxicol.* **1996**, *18*, 342–354. [CrossRef]
3. Webb, R.P. Engineering of botulinum neurotoxins for biomedical applications. *Toxins* **2018**, *10*, 231. [CrossRef] [PubMed]
4. Masuyer, G.; Chaddock, J.A.; Foster, K.A.; Ravi Acharya, K. Engineered botulinum neurotoxins as new therapeutics. *Annu. Rev. Pharmacol. Toxicol.* **2014**, *54*, 27–51. [CrossRef] [PubMed]
5. Chen, Z.P.; Glenn Morris, J.; Rodriguez, R.L.; Shukla, A.W.; Tapia-Núñez, J.; Okun, M.S. Emerging opportunities for serotypes of botulinum neurotoxins. *Toxins* **2012**, *4*, 1196–1222. [CrossRef]
6. Hill, K.K.; Xie, G.; Foley, B.T.; Smith, T.J. Genetic diversity within the botulinum neurotoxin-producing bacteria and their neurotoxins. *Toxicon* **2015**, *107*, 2–8. [CrossRef]
7. Tanizawa, Y.; Fujisawa, T.; Mochizuki, T.; Kaminuma, E.; Suzuki, Y.; Nakamura, Y.; Tohno, M. Draft genome sequence of *Weissella oryzae* SG25T, isolated from fermented rice grains. *Genome Announc.* **2014**, *2*, 3–4. [CrossRef]
8. Zhang, S.; Lebreton, F.; Mansfield, M.J.; Miyashita, S.I.; Zhang, J.; Schwartzman, J.A.; Tao, L.; Masuyer, G.; Martínez-Carranza, M.; Stenmark, P.; et al. Identification of a botulinum neurotoxin-like toxin in a commensal strain of Enterococcus faecium. *Cell Host Microbe* **2018**, *23*, 169–176. [CrossRef]
9. Zhang, S.; Masuyer, G.; Zhang, J.; Shen, Y.; Henriksson, L.; Miyashita, S.I.; Martínez-Carranza, M.; Dong, M.; Stenmark, P. Identification and characterization of a novel botulinum neurotoxin. *Nat. Commun.* **2017**, *8*, 14130. [CrossRef]
10. Contreras, E.; Masuyer, G.; Qureshi, N.; Chawla, S.; Dhillon, H.S.; Lee, H.L.; Chen, J.; Stenmark, P.; Gill, S.S. A neurotoxin that specifically targets Anopheles mosquitoes. *Nat. Commun.* **2019**, *10*, 2869. [CrossRef]
11. Montal, M. Botulinum neurotoxin: A marvel of protein design. *Annu. Rev. Biochem.* **2010**, *79*, 591–617. [CrossRef] [PubMed]
12. Dong, M.; Yeh, F.; Tep, W.H.; Chapman, P.; Dean, C.; Johnson, E.A.; Janz, R.; Chapman, E.R. SV2 is the protein receptor for botulinum neurotoxin A. *Science* **2006**, *312*, 592–596. [CrossRef] [PubMed]
13. Oblatt-Montal, M.; Yamazaki, M.; Nelson, R.; Montal, M. Formation of ion channels in lipid bilayers by a peptide with the predicted transmembrane sequence of botulinum neurotoxin A. *Protein Sci.* **1995**, *4*, 1490–1497. [CrossRef]
14. Schmid, M.F.; Robinson, J.P.; Dasgupta, B. Direct visualization of botulinum neurotoxin-induced channels in phospholipid vesicles. *Nature* **1993**, *364*, 827–830. [CrossRef] [PubMed]
15. Hoch, D.H.; Romero-Mira, M.; Ehrlich, B.E.; Finkelstein, A.; DasGupta, B.R.; Simpson, L.L. Channels formed by botulinum, tetanus, and diphtheria toxins in planar lipid bilayers: Relevance to translocation of proteins across membranes. *Proc. Natl. Acad. Sci. USA* **1985**, *82*, 1692–1696. [CrossRef] [PubMed]
16. Dong, M.; Masuyer, G.; Stenmark, P. Botulinum and tetanus neurotoxins. *Annu. Rev. Biochem.* **2019**, *88*, 811–837. [CrossRef] [PubMed]
17. Pirazzini, M.; Tehran, D.A.; Zanetti, G.; Megighian, A.; Scorzeto, M.; Fillo, S.; Shone, C.C.; Binz, T.; Rossetto, O.; Lista, F.; et al. Thioredoxin and its reductase are present on synaptic vesicles, and their inhibition prevents the paralysis induced by botulinum neurotoxins. *Cell Rep.* **2014**, *8*, 1870–1878. [CrossRef] [PubMed]
18. Schiavo, G.; Rossetto, O.; Catsicas, S.; De Laureto, P.P.; DasGupta, B.R.; Benfenati, F.; Montecucco, C. Identification of the nerve terminal targets of botulinum neurotoxin serotypes A, D, and E. *J. Biol. Chem.* **1993**, *268*, 23784–23787. [CrossRef]
19. Pellett, S.; Bradshaw, M.; Tepp, W.H.; Pier, C.L.; Whitemarsh, R.C.M.; Chen, C.; Barbieri, J.T.; Johnson, E.A. The light chain defines the duration of action of botulinum toxin serotype a subtypes. *MBio* **2018**, *9*, e00089-18. [CrossRef]
20. Rossetto, O.; Montecucco, C. Tables of toxicity of botulinum and tetanus neurotoxins. *Toxins* **2019**, *11*, 686. [CrossRef]
21. Whitemarsh, R.C.M.; Tepp, W.H.; Bradshaw, M.; Lin, G.; Pier, C.L.; Scherf, J.M.; Johnson, E.A.; Pellett, S. Characterization of botulinum neurotoxin A Subtypes 1 through 5 by investigation of activities in mice, in neuronal cell cultures, and in vitro. *Infect. Immun.* **2013**, *81*, 3894–3902. [CrossRef] [PubMed]
22. Pellett, S.; Tepp, W.H.; Whitemarsh, R.C.M.M.; Bradshaw, M.; Johnson, E.A. In vivo onset and duration of action varies for botulinum neurotoxin A subtypes 1-5. *Toxicon* **2015**, *107*, 37–42. [CrossRef] [PubMed]
23. Benoit, R.M.; Schärer, M.A.; Wieser, M.M.; Li, X.; Frey, D.; Kammerer, R.A. Crystal structure of the BoNT/A2 receptor-binding domain in complex with the luminal domain of its neuronal receptor SV2C. *Sci. Rep.* **2017**, *7*, 43588. [CrossRef] [PubMed]

24. Gustafsson, R.; Zhang, S.; Masuyer, G.; Dong, M.; Stenmark, P. Crystal structure of botulinum neurotoxin A2 in complex with the human protein receptor SV2C reveals plasticity in receptor binding. *Toxins* **2018**, *10*, 153. [CrossRef] [PubMed]

25. Davies, J.R.; Hackett, G.S.; Liu, S.M.; Acharya, K.R. High resolution crystal structures of the receptor-binding domain of *Clostridium botulinum* neurotoxin serotypes A and FA. *PeerJ* **2018**, *2018*, e4552. [CrossRef]

26. Davies, J.R.; Rees, J.; Liu, S.M.; Acharya, K.R. High resolution crystal structures of Clostridium botulinum neurotoxin A3 and A4 binding domains. *J. Struct. Biol.* **2018**, *202*, 113–117. [CrossRef]

27. Davies, J.R.; Britton, A.; Liu, S.M.; Acharya, K.R. High-resolution crystal structures of the botulinum neurotoxin binding domains from subtypes A5 and A6. *FEBS Open Bio* **2020**, *10*, 1474–1481. [CrossRef]

28. Gregory, K.S.; Liu, S.M.; Acharya, K.R. Crystal structure of botulinum neurotoxin subtype A3 cell binding domain in complex with GD1a co-receptor ganglioside. *FEBS Open Bio* **2020**, *10*, 298–305. [CrossRef]

29. Gregory, K.S.; Mojanaga, O.O.; Liu, S.M.; Acharya, K.R. Crystal structures of botulinum neurotoxin subtypes A4 and A5 cell binding domains in complex with receptor ganglioside. *Toxins* **2022**, *14*, 129. [CrossRef]

30. Veevers, R.; Hayward, S. Biophysics and physicobiology movements in large biomolecular complexes. *Biophys. Phys.* **2019**, *16*, 328–336. [CrossRef]

31. Yowler, B.C.; Schengrund, C.L.; Pennsyl, V. Botulinum neurotoxin A changes conformation upon binding to ganglioside GT1b. *Biochemistry* **2004**, *43*, 9725–9731. [CrossRef] [PubMed]

32. Ruszkowski, M.; Dauter, Z. On methylene-bridged cysteine and lysine residues in proteins. *Protein Sci.* **2016**, *25*, 1734–1736. [CrossRef]

33. Rabe von Pappenheim, F.; Wensien, M.; Ye, J.; Uranga, J.; Irisarri, I.; de Vries, J.; Funk, L.M.; Mata, R.A.; Tittmann, K. Widespread occurrence of covalent lysine–cysteine redox switches in proteins. *Nat. Chem. Biol.* **2022**, *18*, 368–375. [CrossRef] [PubMed]

34. Wang, J. Crystallographic identification of spontaneous oxidation intermediates and products of protein sulfhydryl groups. *Protein Sci.* **2019**, *28*, 472–477. [CrossRef] [PubMed]

35. Ruszkowski, M.; Dauter, Z. Comment on Wang's paper on the covalent Cys-X-Lys bridges. *Protein Sci.* **2019**, *28*, 470–471. [CrossRef]

36. Wensien, M.; von Pappenheim, F.R.; Funk, L.M.; Kloskowski, P.; Curth, U.; Diederichsen, U.; Uranga, J.; Ye, J.; Fang, P.; Pan, K.T.; et al. A lysine–cysteine redox switch with an NOS bridge regulates enzyme function. *Nature* **2021**, *593*, 460–464. [CrossRef]

37. Davies, J.R. Structure-Function Studies on Clostridium Botulinum Neurotoxins. Ph.D. Thesis, University of Bath, Bath, UK, 2019.

38. Waterman, D.G.; Winter, G.; Gildea, R.J.; Parkhurst, J.M.; Brewster, A.S.; Sauter, N.K.; Evans, G. Diffraction-geometry refinement in the DIALS framework. *Acta Crystallogr. Sect. D Struct. Biol.* **2016**, *72*, 558–575. [CrossRef]

39. McCoy, A.J.; Grosse-Kunstleve, R.W.; Adams, P.D.; Winn, M.D.; Storoni, L.C.; Read, R.J. Phaser crystallographic software. *J. Appl. Crystallogr.* **2007**, *40*, 658–674. [CrossRef]

40. Winn, M.D.; Ballard, C.C.; Cowtan, K.D.; Dodson, E.J.; Emsley, P.; Evans, P.R.; Keegan, R.M.; Krissinel, E.B.; Leslie, A.G.W.; McCoy, A.; et al. Overview of the CCP4 suite and current developments. *Acta Crystallogr. Sect. D Biol. Crystallogr.* **2011**, *67*, 235–242. [CrossRef]

41. Vagin, A.A.; Steiner, R.A.; Lebedev, A.A.; Potterton, L.; McNicholas, S.; Long, F.; Murshudov, G.N. REFMAC5 dictionary: Organization of prior chemical knowledge and guidelines for its use. *Acta Crystallogr. Sect. D Biol. Crystallogr.* **2004**, *60*, 2184–2195. [CrossRef]

42. Liebschner, D.; Afonine, P.V.; Baker, M.L.; Bunkoczi, G.; Chen, V.B.; Croll, T.I.; Hintze, B.; Hung, L.W.; Jain, S.; McCoy, A.J.; et al. Macromolecular structure determination using X-rays, neutrons and electrons: Recent developments in Phenix. *Acta Crystallogr. Sect. D Struct. Biol.* **2019**, *75*, 861–877. [CrossRef] [PubMed]

43. Emsley, P.; Lohkamp, B.; Scott, W.G.; Cowtan, K. Features and development of Coot. *Acta Crystallogr. Sect. D Biol. Crystallogr.* **2010**, *66*, 486–501. [CrossRef] [PubMed]

44. Williams, C.J.; Headd, J.J.; Moriarty, N.W.; Prisant, M.G.; Videau, L.L.; Deis, L.N.; Verma, V.; Keedy, D.A.; Hintze, B.J.; Chen, V.B.; et al. MolProbity: More and better reference data for improved all-atom structure validation. *Protein Sci.* **2018**, *27*, 293–315. [CrossRef] [PubMed]

45. Berman, H.; Henrick, K.; Nakamura, H. Announcing the worldwide Protein Data Bank. *Nat. Struct. Biol.* **2003**, *10*, 980. [CrossRef]

46. McNicholas, S.; Potterton, E.; Wilson, K.S.; Noble, M.E.M. Presenting your structures: The CCP4mg molecular-graphics software. *Acta Crystallogr. Sect. D Biol. Crystallogr.* **2011**, *67*, 386–394. [CrossRef]